Molecular Modeling Connect
2025, Vol. 2, Cite as: doi:10.x/journal.x.x.x

SCIFINITI PUBLISHING

OPEN ACCESS

Research Article

Unraveling Conformational Thermodynamics of Ligand Binding to Fluoride Riboswitch Aptamer: Implications for Therapeutic Design

Soumi Das[1*]

[1]**Department of Physics of Complex Systems, S. N. Bose National Centre for Basic Sciences, Salt Lake, Kolkata 700106, India.**

Correspondence: Soumi Das

E-mail: iammandovi@gmail.com

Institutional email address: soumi.das@bose.res.in

ORCID ID: https://orcid.org/0009-0005-2869-5849

Highlights

- Conformational stability of (i) the holo form of T. Petrophila fluoride riboswitch aptamer (RNA+F^- +Mg^{2+}+K^+) with respect to (ii) the apo form of fluoride riboswitch (RNA in the absence of F^-+Mg^{2+}+K^+) is studied using molecular dynamics simulation.
- Holo Fluoride riboswitch aptamer gets energetically and entropically stable at Pseudoknot, Stem1, and Ion recognition sites, whereas Stem2, Loop1, Loop2, and most of the unpaired bases show significant disorder and destabilization.
- The hydrogen bond network for Pseudoknot, Stem1, and Stem2 in the apo Fluoride riboswitch is significantly weak.
- Molecular Docking study confirms that the thermodynamically destabilized and disordered residues in Stem2 and Loop1 of the holo fluoride riboswitch aptamer may act as potential binding sites for non-cognate ligands.

Abstract

Riboswitches are structured non-coding mRNA segments in which ligand binding to an aptamer domain induces conformational changes in a downstream expression platform to regulate gene expression, positioning them as attractive targets for antimicrobial therapy. The fluoride riboswitch, found in several pathogenic bacteria, is a promising yet underexplored target despite evidence of its role in bacterial defense through fluoride ion (F^-) binding in the presence of Mg^{2+}. In this study, we investigate the conformational stability of (i) the holo form of the *Thermotoga petrophila* fluoride riboswitch aptamer (RNA in the presence of F^-+Mg^{2+}+K^+) relative to (ii) the apo form (RNA in the absence of F^-+Mg^{2+}+K^+). Conformational thermodynamic analysis reveals that the holo riboswitch is stabilized by the Ion recognition site, the Pseudoknot, and Stem 1, whereas Stem 2, Loop 1, Loop 2, and most unpaired nucleotides exhibit pronounced disorder and destabilization. Complementary docking studies identify these destabilized regions as putative binding pockets for non-cognate ligands. Together, these findings provide structural and thermodynamic insights into fluoride riboswitch–ligand interactions, guiding the design of nucleic acid–targeted therapeutics, including RNA-modulating drugs and engineered aptamers. Future in vitro and in vivo validation will be critical for translating these computational predictions into novel strategies to combat antimicrobial resistance.

Keywords: fluoride riboswitch aptamer; RNA-ligand interaction; molecular dynamics simulation; conformational thermodynamics; nucleic acid-targeted therapeutics

1. Introduction

Riboswitches are structured RNA elements, typically located in the 5′ untranslated regions of bacterial mRNAs, which regulate gene expression through direct recognition of small metabolites. Ligand binding to the aptamer domain induces conformational changes in the expression platform via conformational selection and induced-fit mechanisms, enabling regulation at the levels of transcription, translation, mRNA stability, or, in some cases, splicing—all without the involvement of protein cofactors.

Riboswitches achieve precise metabolite recognition and regulatory switching through an intricate interplay of conserved secondary motifs and stabilizing tertiary contacts. In the thiamine pyrophosphate (TPP) riboswitch, helices P1–P5 and internal loops form the ligand-binding junction, while coaxial stacking and loop–loop interactions stabilize the pyrophosphate pocket. Purine riboswitches use a streamlined architecture in which the P1 helix serves as the genetic switch. At the same time, bulged residues in P2–P3 define the purine-binding pocket, reinforced by kissing-loop contacts and base triples. A-rich loops and helical scaffolds orient the ligand, while base triples and aromatic stacking stabilize the isoalloxazine ring in the flavin mononucleotide (FMN) riboswitch. The fluoride riboswitch integrates a pseudoknot stem with Mg^{2+} mediated tertiary contacts to stabilize an anion-binding pocket, and the SAM-I riboswitch uses a four-way junction, internal asymmetries, and tertiary A-minor interactions to enclose its sulfonium center. In the glycine riboswitch, long-range loop–loop interactions bridge separate aptamer domains, enabling cooperative binding across two glycine sites. Across diverse riboswitch classes—including FMN, B12 (Cobalamin), and THI-box; T-loop motifs serve as conserved structural modules that mediate long-range tertiary interactions essential for ligand recognition and riboswitch function. Collectively, these examples illustrate a unifying principle of riboswitch biology: secondary elements such as helices, bulges, and pseudoknots provide the structural scaffold, while tertiary interactions—including loop–loop docking, base triples, and metal-mediated contacts—refine the architecture and confer the ligand specificity and precise regulatory control that define riboswitch function.

Dedicated databases are increasingly central to riboswitch research, integrating sequence, structural, and functional information across diverse classes. Ribocentre-switch compiles over 89,000 sequences from 56 riboswitch families and orphan candidates, linking experimentally validated structures with ligand-binding and comparative visualizations. By unifying natural and orphan riboswitches, the platform enables evolutionary analyses, functional annotation, and mechanistic studies. Such resources not only accelerate riboswitch discovery but also provide a foundation for exploiting RNA-based regulatory elements in synthetic biology and biotechnology. To date, over 55 riboswitch classes have been identified, recognizing diverse ligands ranging from coenzymes (e.g., FMN, TPP, SAM, NAD^+), sugars (e.g., glucosamine-6-phosphate), nucleobases and their derivatives (e.g., adenine, guanine, xanthine and prequeuosine1), and amino acids (e.g., glycine, lysine), to signaling molecules (e.g., cyclic AMP-

GMP and cyclic di-GMP) and simple ions such as Mn^{2+}, Mg^{2+}, and F^{-}. Although traditionally viewed as small-molecule sensors, riboswitches can also recognize larger ligands such as tRNAs, as seen in T-box riboswitches, which engage their cognate tRNA at multiple distant sites through diverse RNA–RNA interactions. In addition to gene regulation, some riboswitches function as ribozymes, as exemplified by the glmS riboswitch, which undergoes self-cleavage upon binding glucosamine-6-phosphate, thereby directly linking metabolite sensing with mRNA degradation.

Riboswitches' high specificity, absence in humans, and central roles in essential bacterial pathways—such as coenzyme biosynthesis and amino acid metabolism—make them highly attractive drug targets. Riboswitch-targeted drug design follows three main strategies: (i) developing synthetic analogs that mimic natural ligands to modulate riboswitch activity, (ii) designing ligands that lock the riboswitch in an inactive conformation to block gene regulation, and (iii) using compounds that disrupt ligand binding or interfere with aptamer–expression platform communication to inhibit riboswitch function. Such approaches not only impair bacterial survival but also provide mechanisms distinct from protein-targeting antibiotics, offering strong potential to overcome existing resistance pathways [1-6].

Metalloriboswitches are a subclass of riboswitches that sense specific metal ions and regulate genes involved in metal transport, homeostasis, and detoxification. By binding their cognate ions, these RNAs undergo conformational changes that control transcription or translation, thereby maintaining essential yet potentially toxic metals at optimal levels. Representative examples include the manganese riboswitch (ykoY family) in Bacillus subtilis, which balances Mn^{2+} uptake, the nickel–cobalt riboswitch that activates efflux pumps to prevent Ni^{2+} and Co^{2+} toxicity, and the magnesium riboswitch in Salmonella enterica, which modulates the mgtA transporter. Although not a metal sensor, the fluoride riboswitch is often discussed alongside this group due to its role in controlling anion efflux under toxic conditions. Beyond their physiological importance, metalloriboswitches hold promise as antibacterial drug targets, since disrupting their function perturbs metal balance, and act as biosensors, owing to their natural selectivity for metal ions.

The fluoride riboswitch exemplifies RNA–anion recognition, where three Mg^{2+} ions selectively chelate the highly electronegative F^{-} ion, as illustrated in Fig. 1(a) and (b). This riboswitch maintains cytoplasmic fluoride levels below toxic thresholds and, due to its presence in several human pathogens, represents a potential antimicrobial target. Remarkably, among halides, only F^{-} exhibits strong specificity for the aptamer. The fluoride riboswitch achieves exceptional F^{-} selectivity through a unique metal-mediated coordination, where three Mg^{2+} ions, octahedrally coordinated with water and inward-facing RNA phosphate oxygens, form an electrostatic cage that stabilizes the weakly hydrated anion. This coordination triggers conformational changes in the aptamer that propagate to the expression platform, coupling fluoride recognition to gene regulation. In Bacillus cereus, the riboswitch controls transcription termination, while in Pseudomonas syringae it regulates translation initiation, activating genes for fluoride transporters (e.g., CrcB) and resistant enzymes to preserve cellular homeostasis. Fluoride binding stabilizes a pseudoknot that prevents terminator formation, whereas its absence promotes terminator hairpin formation, creating an Mg^{2+} -assisted two-step switching mechanism central to

regulatory function. Through this coupling of coordination chemistry and RNA folding, the riboswitch links selective fluoride recognition to transcriptional or translational regulation.

Fluoride riboswitches have emerged as highly sensitive and selective biosensors, capable of detecting fluoride ions (F^-) through conformational changes coupled to measurable outputs such as fluorescence or colorimetric signals. This approach offers cost-effective alternatives to conventional detection methods, enabling rapid water quality monitoring. Beyond biomedical applications, fluoride riboswitches are valuable for environmental monitoring and as research tools to study cotranscriptional folding, RNA–ligand interactions, and gene regulation. More broadly, riboswitches are versatile RNA regulators with expanding roles in biosensing and biotherapy, including food safety, metabolic engineering, live-cell imaging, and antibacterial drug discovery [7-14].

Riboswitches control bacterial ion homeostasis by sensing metabolites or ions and regulating gene expression. The fluoride riboswitch aptamer encapsulates F^- via three Mg^{2+} ions, but the assembly mechanism remained unclear. Using multiscale RNA simulations, Kumar et al. (2023) showed that two Mg^{2+} ions initially coordinate Ligand Binding Domain (LBD) phosphates through water-mediated outer-shell interactions before forming dehydrated inner-shell contacts to stabilize the domain. The third Mg^{2+} ion and fluoride bind cooperatively as a water-mediated ion pair, reducing electrostatic repulsion. Stability arises from a finely balanced network of five phosphates, three Mg^{2+} ions, and solvated fluoride, revealing a stepwise assembly mechanism and guiding the design of RNA-based ion sensors and molecular logic devices [8]. Density functional theory (DFT) has elucidated how the Mg^{2+}/fluoride/phosphate/water cluster at the center of the fluoride riboswitch contributes to its stability and specificity (Chawla et al., 2015) [9]. Additionally, molecular dynamics simulations have been utilized to investigate the folding pathways and conformational changes of the riboswitch in response to ligand binding. These computational insights have complemented experimental findings, such as those from single-molecule fluorescence resonance energy transfer (smFRET) studies, which have revealed the dynamic folding transitions of the Bacillus cereus fluoride riboswitch in the presence of fluoride ions. In the fluoride riboswitch, transcriptional repression is driven by a transient excited state (ES). Using 180 μs of molecular dynamics simulations, Hu et al. (2024) mapped the ES ensemble and uncovered a signaling pathway linking the Mg^{2+}/F^- binding pocket to the regulatory A40–U48 pair via U7–G8 phosphate interactions and a G8–C47–U48 nucleobase network. These results provide structural insight into ligand-sensing dynamics and reveal how a holo-like apo conformation primes transcription termination [10]. Collectively, these computational approaches have provided a detailed mechanistic understanding of how fluoride riboswitches function as molecular sensors and regulators, paving the way for their application in synthetic biology and therapeutic development. Experimental studies using SHAPE-seq, CEST-NMR, and smFRET on the Bacillus cereus crcB fluoride riboswitch highlight aptamer stability across different ion states [15-16].

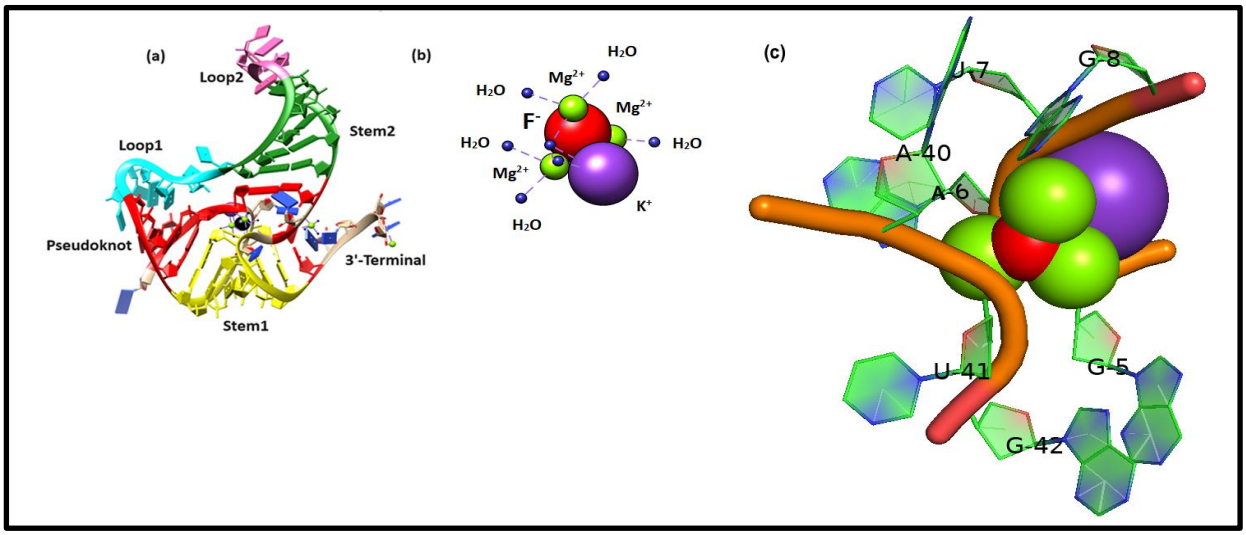

Fig 1(a) Crystal structure of the aptamer domain of Fluoride riboswitch of T. Petrophila (PDB-ID: 4ENC) with K^+ and tri-Mg^{2+} coordination of F^- is shown in cartoon representation. The tertiary structural elements, pseudoknot, stem1, stem2, loop1, loop2, and the 3' terminal are shown in red, yellow, green, cyan, hot pink, and brown, respectively. (b) Coordination scheme of F^- (red), Mg^{2+} (green), and K^+ (violet). The blue sphere indicates coordinated water. (C) Close-up of the ion-binding site in the fluoride riboswitch.

Despite the availability of its experimental structure, the detailed structural and thermodynamic mechanisms of ligand binding remain unresolved. Standard techniques such as Isothermal titration calorimetry (ITC) directly measures the overall thermodynamics of ligand binding, enabling precise determination of key parameters such as binding affinity (K_a), stoichiometry (n), enthalpy change (ΔH), and entropy change (ΔS) but lack residue-specific insight. To address this gap, we evaluated the domain-wise and residue-specific conformational stability of the holo fluoride riboswitch relative to the apo form using a histogram-based thermodynamics approach derived from atomistic molecular dynamics simulations [17-24]. This methodology, previously applied to proteins [17–22] and protein–DNA complexes [23-24], is extended here to RNA. We quantify RNA conformational variables including (i) inter-base pair step parameters (tilt τ, roll ρ, twist ω, shift Dx, slide Dy, rise Dz), (ii) intra-base pair parameters (buckle κ, open σ, propeller π, stagger Sx, shear Sy, stretch Sz), (iii) sugar-phosphate backbone torsions (α, β, γ, δ, ε, ζ) and χ, (iv) sugar pucker (v0–v4), and (v) pseudo-torsions (η, θ). Negative changes in conformational free energy and entropy indicate stabilization and ordering, whereas positive changes reflect destabilization and disorder. RNA conformational variables are described in the Supplementary Information.

Simulating the full expression platform remains challenging due to its intrinsic flexibility and lack of crystallographic data. Ligand removal (F^-, Mg^{2+}, K^+) induces notable phosphate backbone distortions near the binding pocket, as revealed by fluctuations in microscopic conformational variables. It is hypothesized that thermodynamically destabilized and disordered residues serve as additional ligand-binding sites, thereby decreasing the system's free energy and entropy.

Our analyses show that the ion recognition site, pseudoknot, and stem1 are strongly stabilized upon ligand binding, while loop1, loop2, and stem2 become destabilized and disordered. In particular, destabilized regions of stem2 and loop2 may serve as potential sites for non-cognate ligands. Docking

studies with the antibiotics Gramicidin D and Magainin2 support this hypothesis, showing that these ligands preferentially bind to the disordered loop1 and stem2 regions. Overall, our findings reveal residue-wise and domain-wise conformational thermodynamics govern fluoride riboswitch–ligand interactions. This approach can be generalized to investigate non-cognate ligand binding across riboswitches, offering a framework to guide nucleic acid–targeted therapeutic design.

2. Methods

2.1 System preparations

The holo T. petrophila fluoride riboswitch aptamer structure was retrieved from the Protein Data Bank (PDB ID: 4ENC). To construct the apo state, bound fluoride (F^-), magnesium (Mg^{2+}), and potassium (K^+) ions were removed from the crystallographic coordinates. Two different cases of the aptamers are modelled as shown in **Table 1**:

Table 1: Summary of molecular dynamics simulation parameters and structural stability (RMSD) of holo and apo

System	Duration of the Molecular dynamics simulation	Force field	RMSD (mean and SD)
Holo form of fluoride riboswitch (PDB-ID: 4ENC) **(RNA + F^- + Mg^{2+} + K^+)**	1 µs	χ_{OL3} RNA Force field	3.98 Å(0.05)
Apo form of fluoride riboswitch **(Without F^- + Mg^{2+} + K^+)**	1 µs	χ_{OL3} RNA Force field	4.1 Å (0.07)

2.2 Simulation details

All MD simulations are performed using the GROMACS simulation program **[25]** with χ_{OL3} force-field parameters for the RNA **[26].** For explicit solvent calculation, the RNA systems with and without the ligand are solvated in a cubic box with 15 Å thick layers of water molecules and neutralized with the addition of the required number of sodium [Na^+] and chloride [Cl^-] ions. The periodic boundary conditions are imposed in all directions. Subsequently, the systems are energy minimized using the steepest descent algorithm **[27].** Particle Mesh Ewald summation (PME) is used for long-ranged electrostatic interaction with 1 Å grid spacing and 10^{-6} convergence criterion. The Lennard-Jones and the short-range electrostatic interactions are truncated at 10 Å. The all-atom molecular dynamics (MD) simulation is carried out at 300K temperature and 1 atmospheric pressure in an isothermal-isobaric (NPT) ensemble starting from the energy minimized structure. Berendsen thermostat **[28]** is used to keep up a constant temperature and the pressure is controlled by the Parrinello-Rahman barostat **[29].** The LINCS constraints are applied to all bonds involving hydrogen atoms. Integration time step of 1 fs is used. We perform MD simulation for holo and apo Fluoride riboswitch aptamer with 1 µs duration. The trajectories are visualized employing VMD program and images are captured with the help of CHIMERA **[30]** and PYMOL **[31]**.

2.3 Structure analysis

The equilibrations for different systems are judged from the root mean square deviations (RMSD). The backbone phosphorus (P) atom-based root mean square fluctuation (RMSF) per residue is computed to further study the flexibility of each nucleotide and compare the difference in dynamics between unliganded and liganded simulations. Different inter-base and intra-base pair parameters, torsion angle, pseudo-torsion angle, and stacking overlap are calculated using NUPARM software **[32]**. Base pairing information is detected by BPFIND **[33]**.

2.4 Identification of interactions

The interactions are characterized by distance and angle criteria. The hydrogen bonds are taken when the distance between the donor (D) and acceptor (A) is less or equal to 3.5 Å and the angle (D-H-A) cut-off is 160^0. GROMACS Hydrogen bond analysis module is used for hydrogen bond network calculation. Electrostatic interaction is considered when the distance between oppositely charged atoms is less than 5.6 Å.

2.5 Conformational thermodynamics

The detailed description of the histogram-based method (HBM) for calculating the conformational thermodynamics is reported **[17-24]**. The histograms refer to the probability of finding the system in a given conformation. The histograms can be interpreted with the help of the Boltzmann factors corresponding to the effective free energy, and entropy is estimated by the Gibbs Formula. The conformational thermodynamics and the histograms are interconnected in this way. The computations are done using the code in https://github.com/snbsoftmatter/confthermo. The histograms of microscopic conformational variables are computed using equilibrated trajectory, namely, 600 to 1000 ns. The normalized probability distribution of any microscopic conformational variable θ in the free state and the complex state is given by H^{free} (θ) and $H^{complex}$ (θ), respectively. The change in free energy of any microscopic conformational variable θ of the bound state as compared to the free state is defined as,

$$\Delta G_i^{conf}(\theta) = -k_B T \ln\left(H_{max,i}^{complex}(\theta)/H_{max,i}^{free}(\theta)\right)$$

where “max” represents the peak value of the histogram and i represents the RNA residue.

The change in conformational entropy of a given microscopic conformational variable θ of the bound state as compared to the free state is evaluated as,

$$\Delta S_i^{conf}(\theta) = -k_B\left[\sum_j H_{i,j}^{complex}(\theta)\ln H_{i,j}^{complex}(\theta) - \sum_j H_{i,j}^{free}(\theta)\ln H_{i,j}^{free}(\theta)\right]$$

where the sum is taken over all histogram bins j and i represents the RNA residue.

2.6 Docking studies

The average structure of holo Fluoride riboswitch calculated from equilibrated MD trajectory is used as the receptor for the docking procedure, while peptide drugs Gramicidin D and Magainin 2 as ligands. The coordinates of Gramicidin D are extracted from PDB-ID: 1BDW. The coordinates of Magainin 2 are segregated from PDB-ID: 2MAG. At first molecular docking webserver HDOCK **[34],** specialized in protein-protein and protein-DNA/RNA interactions, was used. Next, HADDOCK **[35]** is used for docking to compare the docking score between two structures for two cases. The docking protocol encompasses three stages, namely rigid body energy minimization, semi-flexible simulated annealing in torsion angle space, and explicit solvent refinement. We bias the docking procedure by considering destabilized and disordered residues of loop1 and stem2 of the Fluoride riboswitch aptamer as active residues for binding. The resulting docked structures are sorted by minimum energy criteria and RMSD clustering. The central structure of the cluster with the maximum z-score is selected as the best docked structure. Next, the interface of the docked complex is analyzed based on the distance cut off by 5 Å between residues from the binding partners. We further minimize the docked complexes in the explicit solvent, imposing the steepest descent algorithm, until the maximum force on any atom is less than 100 kJ mol^{-1} nm^{-1} with the Amber protein force field ff14SB for the peptides and χ_{OL3} force-field parameter for the RNA.

3. Results

The equilibrated snapshots of the holo and apo fluoride riboswitch at 1000 ns are shown in **Fig. 2(a) and (b),** respectively. RMSDs of both the holo and apo structure **(Fig. S1 (a))** show variations in RMSD values in an acceptable range; the average RMSD for ligand-free apo structure is 4.1 Å, whereas for the ligand-bound holo-structure, that is 3.98Å. Domain/Region-wise RMSD analysis revealed that the Fluoride riboswitch aptamer exhibited distinct structural flexibility, summarized in **Table S1 (a)**. The equilibrated part of the trajectory (600ns-10000ns) is considered for further analysis.

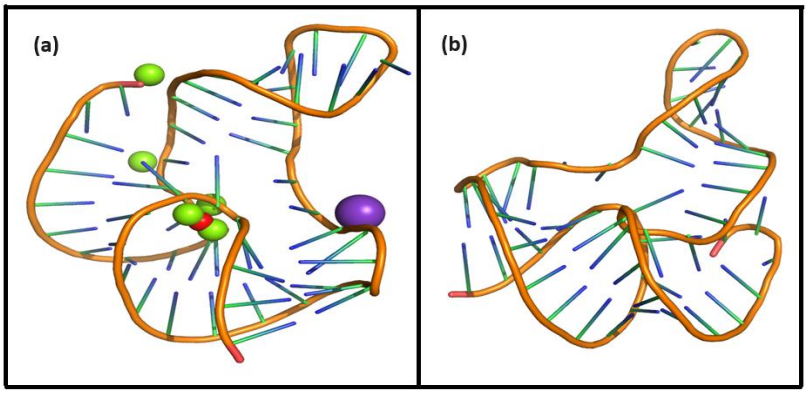

Fig. 2 (a) Holo fluoride riboswitch aptamer domain at 1000 ns. Fluoride (F^-), magnesium (Mg^{2+}), and potassium (K^+) ions are shown as red, green, and purple spheres repectively. (b) Apo fluoride riboswitch aptamer domain at 1000 ns, showing absence of fluoride (F^-); magnesium (Mg^{2+}) and potassium (K^+) ions.

3.1 Global and local dynamics of the aptamer domain and Interaction

The stem1, stem2, pseudoknot, and ligand recognition sites show lower fluctuations for both ligand-free and ligand-bound simulations, as reflected from root mean square fluctuations (RMSF) **(Fig. S1 (b))**. Fluctuations in loop1 (residues 18, 19, 20, 21, 22), loop2 (29, 30, 31, 32), and terminal regions (49, 50, 51, 52) are, in general, higher than in other regions of the aptamer. The free motion of the terminal regions of the aptamer results in relatively higher fluctuations. The fluctuations become more pronounced in apo form with a sharp peak indicating a highly dynamic and flexible loop region. Fluctuations are the least in the ion binding sites (residues 5, 6, 7, 40, 41, 42). On a local scale, local conformational rearrangements in the loop region are manifested by higher RMSF values.

Table S1 (b) compares the probabilities of hydrogen bond interactions in the pseudoknot, stem1, and stem2 regions for the holo and apo systems. Donor-acceptor distance and the donor-hydrogen-acceptor angle cut-off are set as 3.4 Å and 120° ° respectively. Hydrogen bond probabilities P_{HB}> 80% represent Strong (s) hydrogen bonds, while 40% <P_{HB} <80% correspond to Weak (w) hydrogen bonds. The number of Hydrogen bonds is higher in the holo form compared to the apo form. We find that the presence of Mg^{2+} and F^- significantly strengthens almost all Watson-Crick base pair hydrogen bonding interactions in the pseudoknot and stem1 of the holo form. F^- ligand binding to the aptamer domain imposes stabilization of the pseudoknot and inhibits the formation of the terminator hairpin, leading to the transcription of the downstream gene (ON state). On the other hand, weak hydrogen bonds are observed in the holo and apo form of stem2. Watson-Crick base pairing in pseudoknot and stem1 is frequently ruptured in the apo form due to the formation of a transcription terminator (OFF state) involving a stable stem-loop conformation. There occurs a conformational change of the Fluoride riboswitch aptamer occurs in the absence of the cognate ligand F^-. Hydrogen bond analysis thus confirms that the aptamer domain and expression platform of the T. Petrophila Fluoride riboswitch interconvert between two conformations.

The coordination sphere of the ligand binding site is analyzed by the geometric configuration in terms of bond length in the holo system (**Table S1(c), Fig. S2, S3, S4, and S5)**. It is observed from the distance calculation over the MD trajectory that the interaction between Mg1-F and Mg4-F is higher compared to Mg2-F, Mg3-F, and Mg5-F. Average smaller distance (**2Å**) of Mg1-OP1 (7U), Mg1-OP2 (8G), Mg3-OP2 (6A), Mg3-OP2 (7U), Mg3-OP1 (41U), Mg3-OP2 (42G), Mg4-OP1 (6A), and Mg4-OP1 (42G), indicates a strong electrostatic interaction. The distance between Mg^{2+} (1, 2, 3, 4, and 5) and F^- (**Fig. S2 (a), (b), (c), (d) and (e)),** as well as Mg^{2+} and the backbone of Fluoride riboswitch (**Fig. S3, S4, and S5),** remain nearly constant throughout the simulation time indicating stable interaction. Mg^{2+}-backbone distances suggest that Mg^{2+} being an essential constituent of the fluoride riboswitch, forms stable metal coordination site. On the other hand **Table S1(c)** shows that the interaction between K^+ and the backbone of Fluoride riboswitch is highly unstable and dynamic**.** There is no direct interaction between F^- and backbone phosphates of fluoride riboswitch aptamer. The F^- ion is coordinated to three Mg^{2+} ions (Mg1, Mg3, and Mg4), which in turn are chelated to G5pA6pU7pG8 and A40pU41pG42 backbone phosphates and water molecules **(Fig. 1(c))**.

3.2 Structural variability

Base pair parameters and base pair step parameters deliver a great deal of information to assess the overall geometry of the double-helical region of fluoride riboswitch such as pseudoknot, stem1, and stem2 **(Tables S2 (a) and (b), and S3 (a) and (b))**. Roll values are mostly observed as large positive (~10^{o}). In most cases, twist values are around 30^{0}–40^{0}. Slide values are around -1.5 Å in A-form RNA. Rise values are around 3.4 Å in RNA. Base pair parameters and base pair step parameters suggest that most of the base pairs in the pseudoknot and stem regions of holo and apo form of Fluoride riboswitch aptamer predominantly adopt A-form RNA structures with proper stacking between canonical base pairs. Standard deviation values are within acceptable ranges for most of the base pairs, indicating reasonable conformational stabilities. Average roll and twist angles are rather unusual suggesting deformation of some of the steps involving canonical base 5 G:C14 W:W C (pseudoknot), 28 U:A 33 W:W C (stem2) as well as non-canonical base-pairs 21 A:G 3 s:s T (loop1), 38 U:A 6W:W T (pseudoknot) in holo form. On the other hand 20 A:C 17s:s C (loop1), 28 U:A 33 W:W C (stem2), 38 U:A 6 W:W T (pseudoknot) of apo form exhibit significant conformational alteration. Slide value ranges from small positive values to as large as -3 Å for the steps containing non-canonical base-pairs. Buckle, propeller, and stagger values indicate high stability with strong, stable, and planar base pairing of most of the base-pairs in pseudoknot and stem1 of holo and apo form against deformation or rupture of H-bonds. Large open angle is indicative of disruption of the H-bond in loop1 of 20 A:Cs:s C 17, 21 A:Gs:s T 3, and ion recognition site of 41 U:Cs:h T44 for both holo and apo.

Tables S2 (c) and S3 (c) show the backbone torsion angles: χ; pseudo-rotation phase angle (P) and pseudo-torsion angles: η and Θ. The glycosidic torsion angle χ adopts an anti-conformation (+90^{0} to +180^{0}; –90^{0} to –180^{0}) whereas sugar pucker prefers C3'-endo conformation for most of the residues within [0^{0}, 36^{0}] range for fluoride riboswitch aptamer in all two systems. Our data show that A6 (pseudoknot), A19 (loop1), G24 (stem2), G42 (stem1), G52 (terminal residue) of holo and G24 (stem2), G42(stem1), G52 (terminal residue) of apo adopt syn conformation (-90^{0} to+90^{0}). η and θ values are clustered around −170^{0} (-170^{0}+360^{0}=190^{0}) and −140^{0} (-140^{0}+360^{0}=220^{0}) respectively indicating a regular helical-like conformation of pseudoknot, stem1, and stem2. Unusual average η and Θ values are observed in loop and terminal regions for both holo and apo systems with often very high standard deviations. They exhibit C2'-endo pseudorotamer to accommodate the conformational strain. The pseudo-rotation phase angles for all the bases of loop1 and the terminal region show a bimodal or multimodal distribution, indicating higher structural variability.

Table S4 represents the stacking overlap values between two Watson-Crick base pairs in the helical region of pseudoknot, stem1, and stem2 which are found to be around 40-55 $Å^{2}$ indicating significant stacking. Medium amount of stacking is observed between isolated bases in loop1 and loop2. However, non-canonical base pair 20 A: C 17 (s:s C) and 21 A: G 3 (s:s T) of loop1 do not stack well.

3.3 Conformational thermodynamics

We show histograms (**Fig. 3**) for a few conformational variables in different RNA conformations. The most probable value of the corresponding microscopic conformational variable is denoted by the peak of the histogram. $H(\eta_{A6})$ and $H(\eta_{U7})$, the histograms of η for bases A6 (Fig. 3(a)) and U7 (Fig. 3(b)) at the ion recognition site, show that the height of the single-peaked distribution in the holo form is higher than in the apo form, indicating that the flexibility of A6 and U7 is significantly reduced in holo form upon ion binding. $H(\theta_{A19})$ of loop1 (Fig. 3(c)) shifts from a single peak in the apo form to multiple peaks in the holo form, whereas $H(\theta_{C22})$ (Fig. 3(d)) transitions from a double peak in apo to a single peak in holo, reflecting loop-specific conformational rearrangements. $H(v3_{G36})$ of stem2 (Fig. 3(e)) shows single peaks in both states, with increased peak height in holo, consistent with restricted mobility. $H(\theta_{U41})$ and $H(\eta_{G42})$ (Fig. 3(f), 3(g)) are broad in apo but become sharp in holo, indicating reduced conformational fluctuations at the ion recognition site. C50 exhibits bimodal θ distributions in both holo and apo states, $H(\theta_{C50})$, Fig. 3(h), revealing persistent flexibility that may support terminal mobility and overall RNA conformational adaptability.

The sharper and narrower peaks observed for the holo form indicate that ligand binding markedly reduces the conformational flexibility of the fluoride riboswitch. In contrast, broader peaks reflect severe conformational fluctuations, while bimodal distributions highlight transitions between two isomeric conformations. Conversely, sharp unimodal peaks denote conformational stability within a single isomeric state with reduced randomness. Changes in free energy and conformational entropy were quantified by analyzing histograms of all microscopic degrees of freedom in the holo aptamer relative to the apo form.

The relative stability and flexibility of the holo system compared to the apo form are illustrated in a color-coded cartoon representation in Fig. S6. We next discuss the residue-wise (Fig. S7, S8, S9, S10, S11, S12) and domain-wise (Table 2) total changes in conformational thermodynamics ($kJ \cdot mol^{-1}$) of the fluoride riboswitch aptamer. Table 2 illustrates the domain-wise overall changes in conformational thermodynamics (ΔG and TΔS), obtained by summing base pair contributions across all microscopic conformational variables: inter–base pair steps, intra–base pair steps, sugar–phosphate backbone torsion angles, pseudotorsion angles, and sugar pucker.

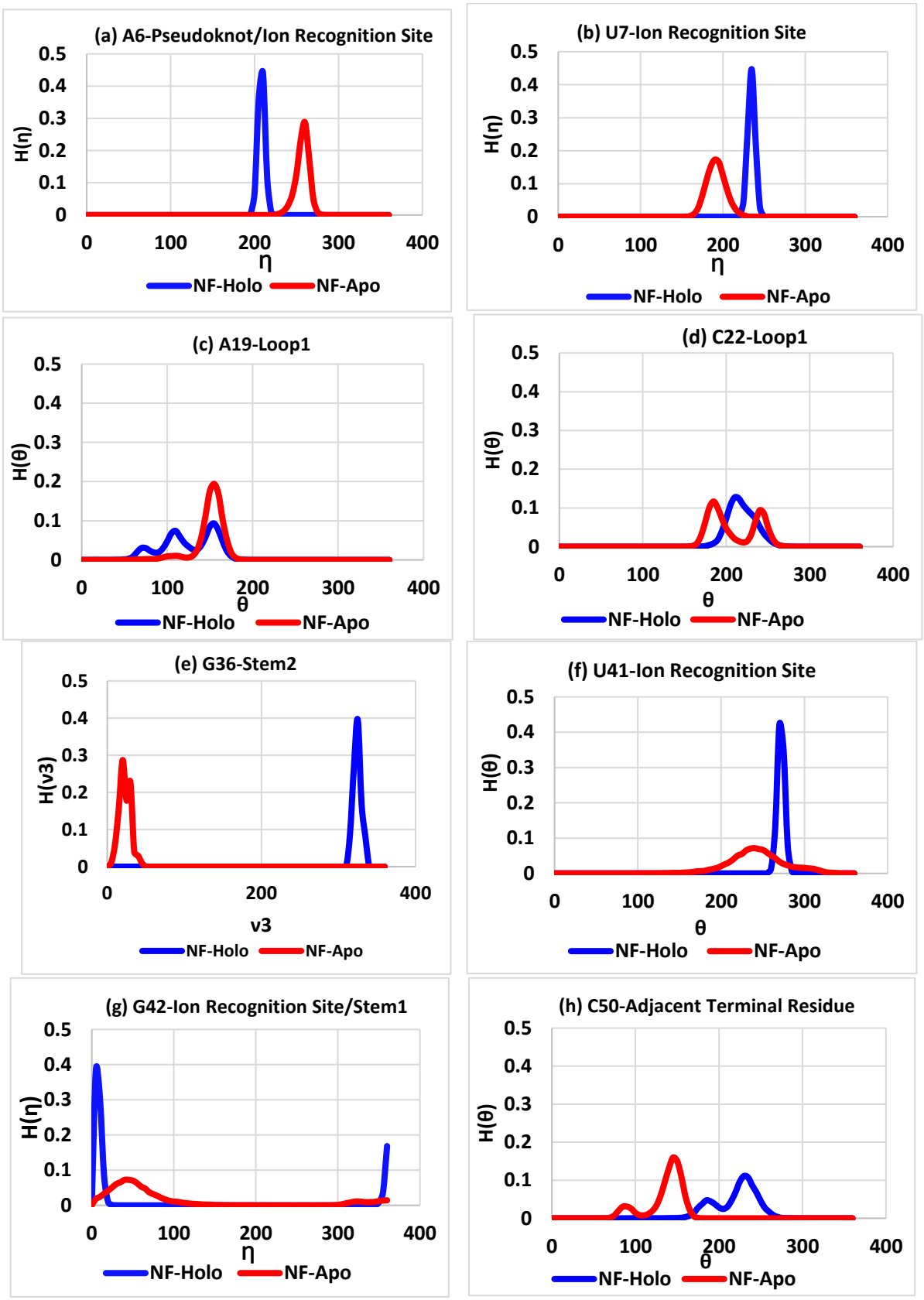

Fig. 3 Histograms of pseudo torsion angles: (a) η of base A6, (b) η of base U7, (c) θ of base A19, (d) θ of base C22, (e) ν3 of base G36, (f) θ of base U41, (g) η of base G42, (h) θ of base C50 for holo and

apo systems in equilibrated trajectories. The solid line indicates the holo system whereas the broken line symbolizes the apo system.

Pseudoknot:

We first consider the conformational thermodynamic changes in free energy ΔG and entropy TΔS caused by inter-bp step parameters (**Fig. S7 (a) and (b)**). Tilt, roll, shift, and rise corresponding to the pseudoknot region do not depend significantly on the base pair steps. On the other hand, twist has maximum stabilization at step G5:C14 and destabilization at A6:U38. We observe that TΔS for all the inter-base-pair step parameters except slide is not sensitive to base pair steps. The step A6:U38 shows the maximum order by slide. The total changes in conformational free energy and entropy for each bp of inter-bp parameters exhibit the highest stabilization and order at A40:U48. Next, we consider the intra-bp step parameters **(Fig. S7 (c) and (d))**. Open, propeller, shear, stagger, and stretch corresponding to the pseudoknot region are not sensitive to bases. The buckle value at A6:U38 exhibits maximum stabilization and order. Finally, total changes in conformational free energy and entropy are computed for each bp of intra-bp parameters. It shows that significant conformational destabilization and disorder at G2:C17, G3:C16, and A40:U48, while maximum stabilization and order at A6:U38.

Torsion angle: α, β, γ, δ, ε, ζ, and χ do not contribute significantly to the bases of the pseudoknot **(Fig. S7 (e) and (f))** except at A6:U38. A6 and U38 show maximum order and stabilization corresponding to the evaluation of the total changes in conformational free energy and entropy over all degrees of freedom of the torsion angle. Next, we shed light on the changes in conformational thermodynamics in terms of pseudo torsion angles **(Fig. S7 (g) and (h))**. ΔG of η and θ at A6 corresponding to (i) holo form with respect to apo form shows maximum stabilization. ΔG and TΔS of θ at C18 contribute maximum destabilization and disorder for the holo form with respect to apo. ΔG of η does not contribute significantly to bases from G15 to C18. We observe that A6 and U38 get highly stabilized and ordered based on the computation of total changes in conformational free energy and entropy in terms of pseudo-torsion angle.

Let us now shed light on the total changes in conformational thermodynamics due to sugar-pucker at pseudoknot **(Fig. S7 (i) and (j))**. ν0, ν1, ν2, ν3 and ν4 do not contribute significantly towards G2, G3, C16 and C17.ν0 exhibits stabilization and order at C4, G5, C14and G15.ν1 shows the significant stabilization and order at bases G5 & C14 whereas ν2 exhibits the highest stabilization and order at A6 and U38. On the other hand, we find that ν0 and ν4has maximum destabilization at A6, and U38.ν3 shows maximum stabilization at base C4 and G15. We evaluate the total changes in conformational free energy and entropy over the sugar torsion angle (ν0, ν1, ν2, ν3, and ν4), which shows the significant stabilization and order at the bases G5, A6, C14, U38, A40, U48, while the most destabilization and disorder is observed at the bases G2, G3, C16 and C17.

Stem1:

At first, we shed light on the changes in conformational thermodynamics in terms of inter-bp step parameters (**Fig S8 (a) and (b)**). Tilt, roll, twist, and shift corresponding to stem1 shows maximum stabilization at the step C12:G43 whereas the steps G8:C47, and A9:U46 are energetically destabilized by roll, twist, and slide. Let us now consider the changes in entropy. TΔS of tilt, roll, slide, and shift are

not sensitive to base steps A9:U46 and G10:C45. On the other hand, rise has most disorder at base step 11G:C44 and C12:G43. Now we evaluate the total changes in conformational free energy and entropy for each bp due to inter-bp step parameters. C12:G43 exhibits maximum stabilization, while maximum destabilization occurs at G10:C45. Total changes in conformation entropy show significant conformational order at G8:C47, C12:G43, and C13:G42. Next, we discuss the changes in conformational thermodynamics due to intra-bp parameters (**Fig. S8 (c) and (d)**). The conformational free energy shows that the open contributes the most to stabilizing the base step C12:G43, while the buckle causes the maximum destabilization at step 11G:C44. Stretch is not sensitive to base steps. ΔG and TΔS of buckle, propeller, and shear contribute the most to stabilizing A9:U46. Evaluation of the total changes in conformational free energy and entropy over the intra-bp parameters exhibits maximum order and stabilization at A9:U46.

ΔG and TΔS of torsion angle do not show sensitivity towards the bases for the holo system **(Fig. S8 (e) and (f))**. Pseudo-torsion angle (η and θ) of ΔG and TΔS do not show sensitivity towards the bases for the holo system except G42 **(Fig. S8 (g) and (h)).** Next, we consider the changes in conformational free energy for sugar-puckers **(Fig. S8 (i) and (j))**. v1, v2 and v4 exhibit significant stabilization at C12 and G43. TΔS is not sensitive to the bases. Computation of the total changes in conformational free energy and entropy indicates the highest disorder and destabilization at A9 and U46, while maximum order and stabilization are observed at C12 and G43.

Stem2:

ΔG for inter-base pair step parameters corresponding to stem2 **(Fig S9 (a) and (b))** are not sensitive to the base pair steps. On the other hand, twist contributes to maximum conformational disorder at the step U28:A33. Next we consider the intra-bp parameters (**Fig S9 (c) and (d)**). The changes in conformational free energy and entropy for the holo system with respect to the apo form do not depend significantly to the bps. The changes in conformational thermodynamics for sugar-phosphate and sugar-base torsion angles are not sensitive to the bases **(Fig S9 (e) and (f))**. The total changes in conformational free energy and entropy indicate that G24, C37, C25, and G36 bases have significant stability and order. ΔG of η has maximum destabilization at U28 and A33. We observe that ΔG of η and θ are not sensitive to the bases from G34 to C37. ΔG and TΔS of θ show destabilization and disorder at C27, U28, and A33 with a maximum value at C27 **(Fig S9 (g) and (h))**. Let us now dicuss on the changes in conformational thermodynamics due to sugar-puckers **(Fig S9 (i) and (j))**. The changes in conformational free energy due to v0 indicate stability of the bases C25, G36, C26, G35, C27, G34. v1, v2, v3 and v4 exhibits destabilization towards all bases belong to stem2. Computation of the total changes in conformational free energy exhibits maximum stabilization at bases C25 and G36 and maximum destabilization at bases C27 and G34. We note that TΔS due sugar-pucker are not sensitive to bases. Total changes in conformational entropy shows maximum order at base C25 and G36 while the maximum disorder is observed at C27 and G34.

Loop1:

We see that ΔG and TΔS of sugar-phosphate backbone torsion angles along with sugar-base torsion angle at all bases corresponding to loop1 are not sensitive to bases **(Fig S10 (a) and (b))**. Calculation

of the total changes in conformational free energy and entropy exhibit the most conformational destabilization and disorder at the base A20. Total ΔG and TΔS show that the most conformational stabilization and order at the base C22.ΔG and TΔS of η show destabilization and disorder at loop1 for holo form with respect to apo **(Fig S10 (c) and (d))**. Holo form with respect to apo form contributes maximum destabilization and disorder at base A21. ΔG and TΔS of η and θ contributes significant stabilization and order at U23. Conformational free energy and entropy for sugar pucker angles corresponding to loop1 of v0, v1, v2, v3, and v4 **(Fig S10 (e) and (f))** do not contribute significantly to the bases. The total changes in conformational thermodynamics due to sugar-puckers show that the most conformational stabilization and order at the base C22 while maximum destabilization and disorder at A20.

Loop2:

Sugar-phosphate backbone torsion angles along with sugar-base torsion angle corresponding to loop2 do not contribute significantly to bases **(Fig S11. (a) and (b))**. Total changes in conformational free energy and entropy show destabilization and disorder at base A31. Next, we shed light on pseudo-torsion angle **(Fig S11. (c) and (d))**. Destabilization of loop2 is reflected from ΔG of η and θ for (i) holo form with respect to apo. TΔS of η and θ show significant destabilization and disorder at base A31 and A32. TΔS of θ exhibit the highest stabilization and order at the base A30 for holo form with respect to apo. We find that for sugar-puckers, base A31 has maximum destabilization and disorder **(Fig S11. (e) and (f))**.

Ion recognition site:

Now we examine the conformational thermodynamics due to sugar-phosphate, sugar-base, and sugar-pucker torsion angles at all bases corresponding to the ion recognition site of Fluoride riboswitch aptamer. OP1/OP2 of P_6, P_7, P_8, P_{41} and P_{42} of RNA participate in coordination to Mg^{2+} (1, 3, 4). Mg^{2+} (2) is coordinated with OP2 of P_{40} while for Mg^{2+} (5), the coordinating residue is O2' of P_{52}. K^+ is coordinated with OP1 of P_5, P_6, P_7. The rest of the coordination in all the cases is fulfilled by water molecules. Sugar base torsion angle along with sugar-phosphate torsion angles shows ordering and stabilization at all bases corresponding to the ion recognition site **(Fig S12 (a) and (b))**. The total changes in conformational free energy and entropy indicate the maximum value at A6 and U41. We now discuss the changes in conformational thermodynamics in terms of pseudo torsion angles **(Fig S12 (c) and (d))**. We observe that ΔG and TΔS of η and Θ at A6, 7U, and A40 corresponding to holo form with respect to apo form show significant stabilization and order while the highest stabilization ΔG and ordering (TΔS) Θ at U41 and for η it is G42. Next, we shed light on the conformational thermodynamics for sugar pucker angles **(Fig S12 (e) and (f))**. v0, v1 and v4 exhibit maximum contribution to stabilize the A40 observed from ΔG value. ΔG of v2 and v3 contribute the most at U41. TΔS of v0, v1, v2, v3 and v4 have maximum ordering at U41. Computation of the total changes in conformational free energy and conformational entropy over all sugar-puckers show that G8 has the maximum destabilization and disorder while most stabilization and order are observed at A6 and U41.

Table 2(a) The changes in conformational thermodynamics of the Pseudoknot region of the holo system in comparison to the apo system (kJ/mol).

Pseudoknot	Inter Base-pair	Intra Base-pair	Torsion-angle	Pseudotorsion-angle	Sugar-angle	Total
ΔG(KJ/mol)	-3.39	2.13	-9.81	-6.01	-7.56	-24.64
TΔS (KJ/mol)	-9.05	0.45	-12.29	-6.59	-7.77	-35.25

Table 2(b) The changes in conformational thermodynamics of the Stem1 region of the holo system in comparison to the apo system (kJ/mol).

Stem1	Inter Base-pair	Intra Base-pair	Torsion-angle	Pseudotorsion-angle	Sugar-angle	Total
ΔG(KJ/mol)	-7.57	-1.53	-0.75	-8.68	-4.26	-22.79
TΔS (KJ/mol)	-9.98	-5.73	-0.44	-10.45	-1.14	-27.74

Table 2(c) The changes in conformational thermodynamics of the Stem2 region of the holo system in comparison to the apo system (kJ/mol).

Stem2	InterBase-pair	IntraBase-pair	Torsion-angle	Pseudotorsion-angle	Sugar-angle	Total
ΔG(KJ/mol)	0.92	5.46	1.80	-0.14	2.73	10.77
TΔS (KJ/mol)	4.04	7.57	1.12	-0.29	-0.39	12.05

Table 2(d) The changes in conformational thermodynamics of the Loop1 region of the holo system in comparison to the apo system (kJ/mol).

Loop1	Torsion-angle	Pseudotorsion-angle	Sugar-angle	Total
ΔG(KJ/mol)	14.13	4.05	3.14	21.32
TΔS (KJ/mol)	23.74	5.51	2.47	31.72

Table 2(e) The changes in conformational thermodynamics of the Loop2 region of the holo system in comparison to the apo system (kJ/mol).

Loop2	Torsion-angle	Pseudotorsion-angle	Sugar-angle	Total
ΔG(KJ/mol)	2.55	1.56	-0.14	3.97
TΔS (KJ/mol)	3.26	1.86	1.69	6.81

Table 2(f) The changes in conformational thermodynamics of the Ion recognition site region of the holo system in comparison to the apo system (kJ/mol).

Ion recognition site	Torsion-angle	Pseudotorsion-angle	Sugar-angle	Total
ΔG(KJ/mol)	-23.01	-20.85	-15.77	-59.63
TΔS (KJ/mol)	-30.09	-23.39	-17.67	-71.15

Table 2 (a-f) shows significant stabilization in pseudoknot, stem1, and ion recognition site of the holo form with respect to the apo form. The intra-base pair is the primary factor to destabilize the holo system compared to the apo form, while the inter-base pair, torsion, pseudo-torsion, and sugar angle degrees of freedom are the main factors to stabilize the holo form over the apo form in the pseudoknot region. We find that most of the changes in conformational free energy and entropy are insignificant compared to the thermal energy (≈2.5 kJ/mol) at room temperature for the intra-base pair of the pseudoknot. The intra-base pair is also the main factor to destabilize stem2, whereas pseudo-torsion angle and inter-base pairs are the key factors to stabilize the stem1 of the holo system. We observe that loop1 and stem2 get significantly destabilized. We find that most of the changes for loop2 in conformational free energy and entropy (contribution from torsion angle, pseudo-torsion angle, and sugar angle) are

insignificant compared to the thermal energy (≈2.5 kJ/mol) at room temperature. These observations indicate that specific base pair interactions and backbone torsional degrees of freedom collectively govern the conformational thermodynamics underlying riboswitch function.

4. Discussion

Recent advances in riboswitch research increasingly integrate experimental data with advanced computational modeling to elucidate ligand recognition and accelerate inhibitor discovery. Aboul-ela et al. (2015) provided a seminal framework linking aptamer–ligand interactions to expression platform dynamics, establishing the mechanistic foundation for rational riboswitch engineering [36]. Computational approaches now play a central role, with studies by Wakchaure et al. (2020, 2021, 2022) and Jana et al. (2020) employing molecular dynamics (MD) and well-tempered metadynamics to dissect ligand binding in FMN, TPP, and PreQ1 riboswitches, yielding atomistic insights to guide ligand analog design [37-40]. Elkholy et al. (2024) further demonstrated how structure-based virtual screening and multistage computer-aided drug discovery (CADD) can identify SAM-I riboswitch inhibitors, while Antunes et al. (2025) expanded this toolkit to probe guanosine-analog binding in the 2′-deoxyguanosine-II riboswitch, highlighting riboswitch plasticity and specificity. In the adenine riboswitch, ligand binding to the aptamer domain induces an open-to-closed conformational switch that remodels the expression platform and regulates gene expression. Guodong et al. (2020) showed that this process is governed not only by binding affinity but also by pocket dynamics, with purine and pyrimidine analogues displaying distinct electrostatic contributions and pyrimidines accommodated by a more flexible pocket [41, 42]. Ligand binding modulates transitions between open and closed states, defined by key nucleotide interactions (U51/A52 vs. C74/C75). These results suggest that the dynamical character of the binding pocket strongly influences riboswitch biofunction. Thus, effective ligand design must consider both binding affinity and the conformational adaptability of the pocket. Collectively, these studies underscore a progress from foundational mechanistic modeling to increasingly sophisticated computational pipelines that combine enhanced sampling molecular dynamics, quantum chemical calculations, and AI-driven CADD approaches, positioning riboswitches as promising RNA drug targets and synthetic biology tools [36-42].

The healthcare system faces a profound challenge in managing life-threatening bacterial infections due to the accelerating emergence of antibiotic resistance. This growing threat necessitates the development of next-generation antibiotics with novel mechanisms of action to effectively counter multidrug-resistant pathogens [43]. A recent development involves an artificial cell–based sensor in which a fluoride riboswitch is encapsulated within lipid vesicles [44]. The antibacterial activities of peptides Gramicidin D and Magainin 2 are enhanced in the presence of fluoride ions [45]. This suggests that combination therapy using a conventional antibiotic alongside a toxic anion such as fluoride, which exhibits antibacterial properties, could be an effective strategy. Ovarian cancer (OC) is highly lethal, with few early detection options and limited treatments. Drug repositioning represents a rapid and cost-effective therapeutic strategy. Gramicidin, an antibiotic with anticancer activity, has shown potential to

suppress OC growth by inducing apoptosis. Choi et al. (2023) highlight gramicidin as a promising candidate for further therapeutic exploration in OC [46]. Magainin 2, a pore-forming antimicrobial peptide, exerts its antibacterial effect by inducing bacterial apoptosis-like death [47].

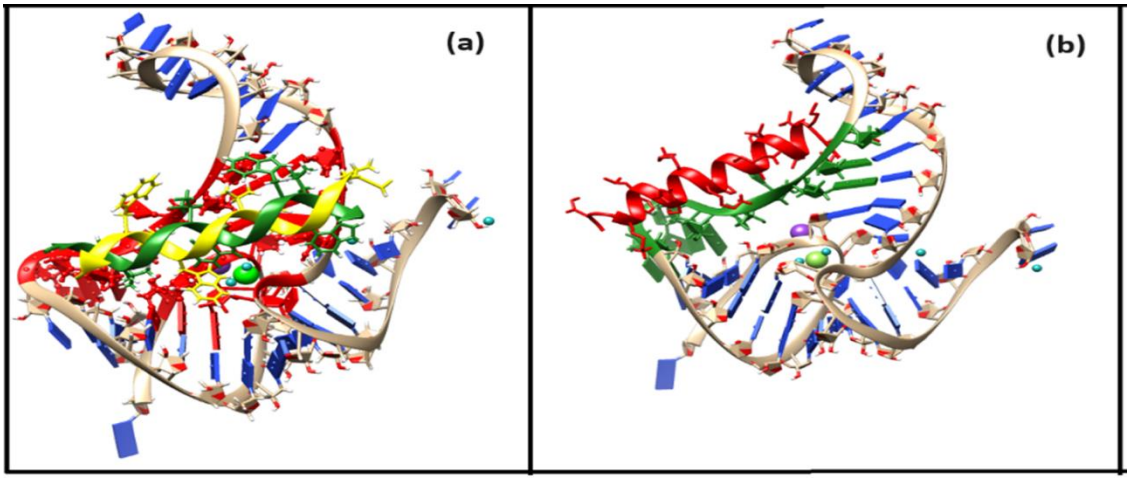

Fig. 4: Docked complex of (a) double-stranded (each helix in green and yellow) GramidinD and Fluoride riboswitch (holo) (b) Magainin 2 (red) and Fluoride riboswitch (holo). Binding sites in the receptor Fluoride riboswitch are depicted in (a) red, (b) green

We discuss the binding mode and interaction pattern of two known peptide antibiotics, Gramicidin D and Magainin 2 peptides, towards Fluoride Riboswitch. We further investigate whether destabilized and disordered regions of the holo fluoride riboswitch could act as docking sites for Gramicidin D and Magainin 2, thereby identifying potential structural hotspots for therapeutic targeting. The docked complexes are represented in Fig. 4a for Gramicidin D and Fig. 4b for Magainin 2.

Gramicidin D binding:

Gramicidin D is a linear pentadeca-peptide antibiotic with alternating L and D amino acids. Residues G5, G15, C16, C17, U38 of Pseudoknot, G24, C25, C26, C27, C37 of Stem2, A 21, 22C, 23U of Loop1, 5G, 6A, 7U, 41U, 42G of Ion Recognition Site of holo Fluoride riboswitch act as receptor interface for peptide antibiotic Gramicidin D which is confirmed from conformational thermodynamics data and HDOCK result. Later, we perform a biased docking analysis with HADDOCK, considering disordered residues A21, C22, U23, G24, C25, C26, and C27 as the active residues of the Fluoride riboswitch. Residues FVA1, DVA6, Val7, Trp11, DLE12, Trp13 of chain A and Ala3, DLE4, DVA8, Trp9, DLE10, Trp13, DLE14, Trp15 of chain B of Gramicidin D, which are found to lie in the vicinity (-4.5Å), act as ligand interface for receptor Fluoride riboswitch. Interfacial residues from Gramicidin D show significant hydrophobic interaction.

Magainin2 binding:

The Hebrew word "magain" means "shield". Conformational thermodynamics data and HDOCK result ensure that destabilized and disordered residues C18, A19, A20, A21, C22, U23 of loop1, 24G, 25C, 26C, 27C, 28U, A33, G34, G35, G36, C37 of stem2 of holo Fluoride riboswitch act as receptor interface. A biased docking analysis with HADDOCK has been performed with Fluoride riboswitch and Magainin

2 considering these destabilized and disordered residues of loop1 and stem2 as the active residues of Fluoride riboswitch. Residues Lys4, Phe5, Ser8, Lys11, Phe12, Lys14, Ala15, Phe16, Gly18, Glu19, Ile20, Met21, Asn22, Ser23 of Magainin 2 which are found to lie in the vicinity (-4.5Å) act as ligand interface for receptor Fluoride riboswitch. Interfacial residues Ala, Gly, Ile, Met, and Phe from Magainin 2 show significant hydrophobic interaction, whereas Lys and Ser undergo dominant electrostatic interaction with Fluoride riboswitch.

Docking score from HDOCK **(Table S5 (a))** as well as HADDOCK **(Table S5 (b))** demonstrate that *the Docked complex of Gramidin D* has a stronger binding affinity for *Fluoride riboswitch* than that of Magainin 2. HADDOCK result illustrates Van der Waals energy as well as electrostatic energy favour the peptide-RNA complex formation, while desolvation energy has less impact on it. Fig. **S13** presents the zoomed view of the interface of the energy-minimized docked complexes. We further dock the peptide drugs Gramicidin D and Magainin 2 to the average simulated structure of the apo Fluoride riboswitch. We show the energy values upon minimization (**Fig. S14 (a) and (b)**) for the docked complexes. The minimum energy for the apo Fluoride riboswitch-Gramicidin D complex and the apo Fluoride riboswitch-Magainin 2 complex is considerably higher than the holo Fluoride riboswitch-Gramicidin D complex and the holo Fluoride riboswitch-Magainin 2 complex. Thus, we find that peptide drug binding to holo Fluoride riboswitch is more favourable compared to apo Fluoride riboswitch.

The Fluoride riboswitch achieves ligand recognition through a tightly packed RNA fold and a network of Mg^{2+} ions rather than extensive (F^-) ligand–RNA hydrogen bonding, reducing opportunities for small-molecule mimicry. Its natural ligand, the simple inorganic anion F^-, possesses extremely high solvation energy and minimal chemical complexity, rendering competitive ligand design inherently challenging (Ren et al., 2012). The high electrostatic potential of the cognate ligand binding site and the dominant role of metal-mediated interactions pose barriers for conventional small-molecule screening pipelines. On the other hand, Peptides offer a larger interaction surface, enabling more extensive and specific contacts with RNA and increasing their potential for high-affinity binding. Together, these factors underscore the need for unconventional strategies—such as RNA-binding macrocycles or allosteric modulators—over traditional small-molecule drugs.

Chimeric antisense oligonucleotides (ASOs) represent a promising strategy to address antimicrobial resistance (AMR) by targeting essential bacterial riboswitches, including glmS, FMN, TPP, and SAM-I. Conjugated with cell-penetrating peptides such as pVEC, these ASOs efficiently enter bacterial cells and bind to riboswitch mRNA, inducing RNase H–mediated degradation [48]. This selective mechanism suppresses bacterial growth while sparing human cells, offering a safe and adaptable platform for antibiotic development. By enabling the design of narrow- or broad-spectrum agents, riboswitch-targeted ASOs hold significant potential against multidrug-resistant pathogens. Advances in macrocyclic peptide discovery (Pal et al., 2022) indicate that riboswitch–peptide interactions are biochemically feasible, though they remain largely synthetic or hypothetical and have not been observed in nature. Owing to their constrained structures, macrocyclic peptides have emerged as promising modulators of protein–protein interactions and could potentially be engineered to target RNA elements

such as riboswitches. However, their application to riboswitches remains nascent, with most studies focusing on synthetic constructs rather than naturally occurring systems [49–50].

Backbone torsions and sugar puckers dictate conformational flexibility and folding in RNA molecular dynamics simulations. The observed variations in torsions are highly dependent on the force field employed, because force fields define the torsional potential energy surfaces and the relative stability of different conformers. Different RNA force fields—such as AMBER ff99bsc0χOL3 and CHARMM36 can produce markedly different populations of backbone and sugar puckers, affecting base-stacking, loop flexibility, and tertiary interactions. Consequently, discrepancies in torsional sampling are often more reflective of force field parameterization than intrinsic RNA dynamics, emphasizing the need for careful force field selection and validation against experimental data such as NMR or crystallography [51-58].

Molecular dynamics simulations of the fluoride riboswitch were performed using the AMBER ff99bsc0 χOL3 force field, widely employed for RNA to capture backbone conformations and topology accurately. This approach allowed us to model the dynamic behaviour of the riboswitch and examine ligand interactions at the atomistic level. However, it is important to note that standard additive force fields like ff99bsc0 χOL3 have inherent limitations, particularly in describing RNA–ion interactions. Fixed-charge models neglect polarization and charge transfer effects, which can impact the coordination and dynamics of divalent cations such as Mg^{2+}, critical for fluoride binding and stabilization of the riboswitch tertiary structure. Additionally, slow ion-binding events and correlated ion–ion interactions are difficult to capture with conventional MD timescales, potentially limiting the accuracy of predicted ion positions and binding energetics. Slow ion-binding dynamics, errors in crystallographic ion placement, and oversimplified bulk ion effects further hinder accurate modeling of RNA. Despite these constraints, the simulations provide valuable mechanistic insights into the fluoride riboswitch's conformational landscape and serve as a foundation for rational ligand design, guiding both experimental validation and future computational refinements. By emphasizing thermodynamic principles, our approach provides a rigorous framework for identifying functional residues, especially in systems where NMR or crystallographic data are unavailable, thereby extending its applicability to a wider range of biomolecular studies [59-63]. These results underscore how geometry and thermodynamics jointly govern function and ligand recognition of riboswitch.

Computational predictions of riboswitch–ligand interactions require experimental validation to confirm biological relevance. Isothermal titration calorimetry (ITC) can precisely quantify ligand binding affinities and thermodynamic parameters, providing a direct complement to docking simulations. Microscale thermophoresis (MST) and fluorescence titration assays enable medium-throughput screening of multiple ligand candidates, facilitating efficient prioritization for detailed studies. Ligand-induced RNA conformational dynamics can be mapped using in-line probing and single-molecule FRET (smFRET), capturing structural transitions under physiological conditions. For atomic-level validation, high-resolution X-ray crystallography and solution NMR spectroscopy can confirm predicted binding poses. Finally, transcription termination assays and cell-based reporter systems will assess functional efficacy

by demonstrating riboswitch-mediated regulation in vitro and in vivo. Collectively, these complementary methods establish a rigorous pipeline for validating computer-aided drug design (CADD) strategies targeting riboswitches [64-75].

5. Conclusion

In summary, our study provides a detailed molecular-level characterization of ligand recognition by the fluoride riboswitch, advancing our understanding of nucleic acid structure–function relationships. Conformational thermodynamic analysis of the holo form with respect to apo forms revealed that structural elements such as the pseudoknot, Stem1, and ion coordination sites confer energetic and entropic stability, whereas Loop1, Loop2, Stem2, and unpaired nucleotides exhibit significant disorder and destabilization. Critical interactions, including the pseudoknot-like reversed Watson–Crick A6•U38 and reversed Hoogsteen A40•U48 base pairs, underpin the riboswitch's higher-order architecture. Importantly, thermodynamically destabilized residues in Loop1 and Stem2 represent promising sites for non-cognate ligand engagement. These insights not only deepen our fundamental understanding of RNA–ligand interactions but also provide a rational framework for designing nucleic acid–based ligands and aptamers, supporting the development of targeted therapeutics that exploit riboswitch-mediated regulatory mechanisms.

List of abbreviations:

- AMP – Adenosine monophosphate
- ATP – Adenosine triphosphate (implied in riboswitch context, though not explicitly written)
- BPFIND – Base Pair FINDer (software)
- CEST-NMR – Chemical Exchange Saturation Transfer – Nuclear Magnetic Resonance
- CHIMERA – UCSF Chimera molecular modeling software
- DFT – Density Functional Theory
- FMN – Flavin mononucleotide
- GROMACS – GROningen MAchine for Chemical Simulations (MD package)
- HADDOCK – High Ambiguity Driven protein–protein Docking
- HBM – Histogram-Based Method
- HDOCK – Hybrid protein–protein Docking webserver
- ITC – Isothermal Titration Calorimetry
- LBD – Ligand Binding Domain
- LINCS – Linear Constraint Solver (MD algorithm)
- MD – Molecular Dynamics
- mRNA – Messenger RNA
- NAD^+ – Nicotinamide adenine dinucleotide (oxidized form)
- NMR – Nuclear Magnetic Resonance
- PME – Particle Mesh Ewald
- PYMOL – Python Molecular Graphics System
- SAM – S-adenosyl methionine
- smFRET – Single-molecule Fluorescence Resonance Energy Transfer
- tRNA – Transfer RNA
- VMD – Visual Molecular Dynamics

Abbreviations of non-canonical base pairs

- W: WT involves Watson–Crick edges of both bases in a trans orientation, commonly referred to as a reverse Watson–Crick base pair.
- H: WT involves the Hoogsteen edge of the first base pairing with the Watson–Crick edge of the second base in a trans orientation.
- s: sC involves Sugar edges of both bases pair in a cis orientation, forming a weak, non-polar C–H…N hydrogen bond.
- s: sT involves Sugar edges of both bases pair in a trans orientation, also forming a weak, non-polar C–H…N hydrogen bond.
- s: hT involves Sugar edge of the first base pairs with the Hoogsteen edge of the second base in trans orientation, forming a weak, non-polar C–H…N hydrogen bond.

Abbreviations of structural elements of Fluoride riboswitch

- PK: Pseudoknot
- P1: Stem1
- P2: Stem2
- L1: Loop1
- L2: Loop2

Author Contributions

Dr. Soumi Das Conceptualization, Methodology, Formal analysis, Investigation, Resources, Data curation, Writing—original draft, Writing—review & editing, Visualization, Supervision

Availability of Data and Materials

Data supporting the results of this study are available upon request from the corresponding author.

Conflicts of interest

There are no conflicts to declare.

Funding: No external funding was received for this research.

Acknowledgments

Dr. Soumi Das acknowledges the Technical Research Centre at S. N. Bose National Centre for Basic Sciences, Kolkata, for computational support, and the Department of Science and Technology (DST) for Postdoctoral Fellowship.

Supplementary Material

Supplementary material associated with this article has been published online and is available at: Link to the DOI

References

[1] Huang, L.; Lilley, D. M. J. Some general principles of riboswitch structure and interactions with small-molecule ligands. Quarterly Reviews of Biophysics 2025, 58. https://doi.org/10.1017/s0033583525100012.

[2] Kavita, K.; Breaker, R. R. Discovering riboswitches: the past and the future. Trends in Biochemical Sciences 2022, 48 (2), 119–141. https://doi.org/10.1016/j.tibs.2022.08.009.

[3] Ellinger, E.; Chauvier, A.; Romero, R. A.; Liu, Y.; Ray, S.; Walter, N. G. Riboswitches as therapeutic targets: promise of a new era of antibiotics. Expert Opinion on Therapeutic Targets 2023, 27 (6), 433–445. https://doi.org/10.1080/14728222.2023.2230363.

[4] Bu, F.; Lin, X.; Liao, W.; Lu, Z.; He, Y.; Luo, Y.; Peng, X.; Li, M.; Huang, Y.; Chen, X.; Xiao, B.; Jiang, J.; Deng, J.; Huang, J.; Lin, T.; Miao, Z.; Huang, L. Ribocentre-switch: a database of riboswitches. Nucleic Acids Research 2023, 52 (D1), D265–D272. https://doi.org/10.1093/nar/gkad891.

[5] Mohsen, M. G.; Breaker, R. R. Prospects for riboswitches in drug development. Methods and Principles in Medicinal Chemistry 2024, 203–226. https://doi.org/10.1002/9783527840458.ch8.

[6] (a) Giarimoglou, N.; Kouvela, A.; Maniatis, A.; Papakyriakou, A.; Zhang, J.; Stamatopoulou, V.; Stathopoulos, C. A Riboswitch-Driven era of new antibacterials. Antibiotics 2022, 11 (9), 1243. https://doi.org/10.3390/antibiotics11091243.

(b) Hansen, L. N.; Kletzien, O. A.; Urquijo, M.; Schwanz, L. T.; Batey, R. T. Context-dependence of T-loop mediated long-range RNA tertiary interactions. Journal of Molecular Biology 2023, 435 (10), 168070. https://doi.org/10.1016/j.jmb.2023.168070.

[7] Ren, A.; Rajashankar, K. R.; Patel, D. J. Fluoride ion encapsulation by Mg2+ ions and phosphates in a fluoride riboswitch. Nature 2012, 486 (7401), 85–89. https://doi.org/10.1038/nature11152.

[8] Kumar, S.; Reddy, G. Mechanism of fluoride ion encapsulation by magnesium ions in a bacterial riboswitch. The Journal of Physical Chemistry B 2023, 127 (43), 9267–9281. https://doi.org/10.1021/acs.jpcb.3c03941.

[9] Chawla, M.; Credendino, R.; Poater, A.; Oliva, R.; Cavallo, L. Structural stability, acidity, and halide selectivity of the fluoride riboswitch recognition site. Journal of the American Chemical Society 2014, 137 (1), 299–306. https://doi.org/10.1021/ja510549b.

[10] Hu, G.; Yu, X.; Li, Z. Unveiling putative excited state and transmission of binding information in the fluoride riboswitch. Journal of Chemical Information and Modeling 2024. https://doi.org/10.1021/acs.jcim.4c00852.

[11] Thavarajah, W.; Silverman, A. D.; Verosloff, M. S.; Kelley-Loughnane, N.; Jewett, M. C.; Lucks, J. B. Point-of-Use detection of environmental fluoride via a Cell-Free Riboswitch-Based biosensor. ACS Synthetic Biology 2019, 9 (1), 10–18. https://doi.org/10.1021/acssynbio.9b00347.

[12] Ariyarathna, M. R.; Nissanka, J. P.; Methlal, K.; Abeyrathne, K. D.; Satharasinghe, M.; Banushan, P.; Manawadu, D.; Arachchilage, G. M.; Silva, G. N. Simple and cost-effective fluoride Riboswitch-Based Whole-Cell biosensor for the determination of fluoride in drinking water. Applied Biochemistry and Biotechnology 2025. https://doi.org/10.1007/s12010-025-05269-2.

[13] Wedekind, J. E.; Dutta, D.; Belashov, I. A.; Jenkins, J. L. Metalloriboswitches: RNA-based inorganic ion sensors that regulate genes. Journal of Biological Chemistry 2017, 292 (23), 9441–9450. https://doi.org/10.1074/jbc.r117.787713.

[14] Wu, Y.; Zhu, L.; Zhang, Y.; Xu, W. Multidimensional applications and challenges of riboswitches in biosensing and biotherapy. Small 2023, 20 (2). https://doi.org/10.1002/smll.202304852.

[15] Zhao, B.; Guffy, S. L.; Williams, B.; Zhang, Q. An excited state underlies gene regulation of a transcriptional riboswitch. Nature Chemical Biology 2017, 13 (9), 968–974. https://doi.org/10.1038/nchembio.2427.

[16] Lee, J.; Sung, S.E.; Lee, J.; Kang, J. Y.; Lee, J. H.; Choi, B. S. Base-Pair Opening Dynamics Study of Fluoride Riboswitch in the Bacillus cereus CrcB Gene. International Journal of Molecular Sciences 2021, 22 (6), 3234. https://doi.org/10.3390/ijms22063234.

[17] Das, A.; Chakrabarti, J.; Ghosh, M. Conformational Contribution to Thermodynamics of Binding in Protein-Peptide Complexes through Microscopic Simulation. Biophysical Journal 2013, 104 (6), 1274–1284. https://doi.org/10.1016/j.bpj.2012.12.058.

[18] Das, A.; Chakrabarti, J.; Ghosh, M. Conformational thermodynamics of metal-ion binding to a protein. Chemical Physics Letters 2013, 581, 91–95. https://doi.org/10.1016/j.cplett.2013.07.022.

[19] Sikdar, S.; Chakrabarti, J.; Ghosh, M. A microscopic insight from conformational thermodynamics to functional ligand binding in proteins. Molecular BioSystems 2014, 10 (12), 3280–3289. https://doi.org/10.1039/c4mb00434e.

[20] Maganti, L.; Ghosh, M.; Chakrabarti, J. Molecular dynamics studies on conformational thermodynamics of Orai1–calmodulin complex. Journal of Biomolecular Structure and Dynamics 2017, 36 (13), 3411–3419. https://doi.org/10.1080/07391102.2017.1388289.

[21] Mondal, M.; Chakrabarti, J.; Ghosh, M. Molecular dynamics simulations on interaction between bacterial proteins: Implication on pathogenic activities. Proteins Structure Function and Bioinformatics 2017, 86 (3), 370–378. https://doi.org/10.1002/prot.25446.

[22] Dutta, S.; Ghosh, M.; Chakrabarti, J. In-silico studies on conformational stability of flagellin–receptor complexes. Journal of Biomolecular Structure and Dynamics 2019, 38 (8), 2240–2252. https://doi.org/10.1080/07391102.2019.1630317.

[23] Mandal, S. C.; Maganti, L.; Mondal, M.; Chakrabarti, J. Microscopic insight to specificity of metal ion cofactor in DNA cleavage by restriction endonuclease EcoRV. Biopolymers 2020, 111 (10). https://doi.org/10.1002/bip.23396.

[24] Kole, K.; Gupta, A. M.; Chakrabarti, J. Conformational stability and order of Hoogsteen base pair induced by protein binding. Biophysical Chemistry 2023, 301, 107079. https://doi.org/10.1016/j.bpc.2023.107079.

[25] Abraham, M. J.; Murtola, T.; Schulz, R.; Páll, S.; Smith, J. C.; Hess, B.; Lindahl, E. GROMACS: High performance molecular simulations through multi-level parallelism from laptops to supercomputers. SoftwareX 2015, 1–2, 19–25. https://doi.org/10.1016/j.softx.2015.06.001.

[26] Zgarbová, M.; Otyepka, M.; Šponer, J.; Mládek, A.; Banáš, P.; Cheatham, T. E.; Jurečka, P. Refinement of the Cornell et al. Nucleic Acids Force Field Based on Reference Quantum Chemical Calculations of Glycosidic Torsion Profiles. Journal of Chemical Theory and Computation 2011, 7 (9), 2886–2902. https://doi.org/10.1021/ct200162x.

[27] Petrova, S. S.; Solov'ev, A. D. The origin of the method of steepest descent. Historia Mathematica 1997, 24 (4), 361–375. https://doi.org/10.1006/hmat.1996.2146.

[28] Lemak, A. S.; Balabaev, N. K. On the Berendsen thermostat. Molecular Simulation 1994, 13 (3), 177–187. https://doi.org/10.1080/08927029408021981.

[29] Saito, H.; Nagao, H.; Nishikawa, K.; Kinugawa, K. Molecular collective dynamics in solid para-hydrogen and ortho-deuterium: The Parrinello–Rahman-type path integral centroid molecular dynamics approach. The Journal of Chemical Physics 2003, 119 (2), 953–963. https://doi.org/10.1063/1.1578474.

[30] Pettersen, E. F.; Goddard, T. D.; Huang, C. C.; Couch, G. S.; Greenblatt, D. M.; Meng, E. C.; Ferrin, T. E. UCSF Chimera—A visualization system for exploratory research and analysis. Journal of Computational Chemistry 2004, 25 (13), 1605–1612. https://doi.org/10.1002/jcc.20084.

[31] Schrödinger, L. & De Lano, W., 2020. *PyMOL*, Available at: http://www.pymol.org/pymol

[32] Bansal, M.; Bhattacharyya, D.; Ravi, B. NUPARM and NUCGEN: software for analysis and generation of sequence dependent nucleic acid structures. Bioinformatics 1995, 11 (3), 281–287. https://doi.org/10.1093/bioinformatics/11.3.281.

[33] Das, J.; Mukherjee, S.; Mitra, A.; Bhattacharyya, D. Non-Canonical base pairs and higher order structures in nucleic acids: Crystal Structure Database analysis. Journal of Biomolecular Structure and Dynamics 2006, 24 (2), 149–161. https://doi.org/10.1080/07391102.2006.10507108.

[34] Yan, Y.; Zhang, D.; Zhou, P.; Li, B.; Huang, S.-Y. HDOCK: a web server for protein–protein and protein–DNA/RNA docking based on a hybrid strategy. Nucleic Acids Research 2017, 45 (W1), W365–W373. https://doi.org/10.1093/nar/gkx407.

[35] Van Zundert, G. C. P.; Rodrigues, J. P. G. L. M.; Trellet, M.; Schmitz, C.; Kastritis, P. L.; Karaca, E.; Melquiond, A. S. J.; Van Dijk, M.; De Vries, S. J.; Bonvin, A. M. J. J. The HADDOCK2.2 Web Server: User-Friendly Integrative modeling of biomolecular complexes. Journal of Molecular Biology 2015, 428 (4), 720–725. https://doi.org/10.1016/j.jmb.2015.09.014.

[36] Aboul-ela, F.; Huang, W.; Elrahman, M. A.; Boyapati, V.; Li, P. Linking aptamer-ligand binding and expression platform folding in riboswitches: prospects for mechanistic modeling and design. Wiley Interdisciplinary Reviews - RNA 2015, 6 (6), 631–650. https://doi.org/10.1002/wrna.1300.

[37] Wakchaure, P. D.; Jana, K.; Ganguly, B. Structural insights into the interactions of flavin mononucleotide (FMN) and riboflavin with FMN riboswitch: a molecular dynamics simulation study. Journal of Biomolecular Structure and Dynamics 2019, 38 (13), 3856–3866. https://doi.org/10.1080/07391102.2019.1665587.

[38] Jana, K.; Wakchaure, P. D.; Ghosh, S.; Bandyopadhyay, T.; Ganguly, B. Quantum chemical and well-tempered metadynamics study to design adenine analogs for orthogonal Preq1 riboswitch. Journal of Biomolecular Structure and Dynamics 2019, 38 (15), 4635–4643. https://doi.org/10.1080/07391102.2019.1682675.

[39] Wakchaure, P. D.; Ganguly, B. Molecular level insights into the inhibition of gene expression by thiamine pyrophosphate (TPP) analogs for TPP riboswitch: A well-tempered metadynamics simulations study. Journal of Molecular Graphics and Modelling 2021, 104, 107849. https://doi.org/10.1016/j.jmgm.2021.107849.

[40] Wakchaure, P. D.; Ganguly, B. Deciphering the mechanism of action of 5FDQD and the design of new neutral analogues for the FMN riboswitch: a well-tempered metadynamics simulation study. Physical Chemistry Chemical Physics 2021, 24 (2), 817–828. https://doi.org/10.1039/d1cp01348c.

[41] Elkholy, N.; Hassan, R.; Bedda, L.; Elrefaiy, M. A.; Arafa, R. K. Exploration of SAM-I Riboswitch Inhibitors: in-Silico Discovery of Ligands to a new Target Employing Multistage CADD Approaches. Artificial Intelligence Chemistry 2024, 2 (1), 100044. https://doi.org/10.1016/j.aichem.2024.100044.

[42] (a) Antunes, D.; Santos, L. H. S.; Caffarena, E. R.; Guimarães, A. C. R. Structural and dynamic properties of guanosine-analog binding to 2′-deoxyguanosine-II riboswitch: a computational study. Journal of Biomolecular Structure and Dynamics 2025, 1–22. https://doi.org/10.1080/07391102.2025.2530092.

(b) Hu, G.; Li, H.; Xu, S.; Wang, J.; Ligand Binding Mechanism and Its Relationship with Conformational Changes in Adenine Riboswitch. International Journal of Molecular Sciences 2020, 21 (6), 1926. https://doi.org/10.3390/ijms21061926.

[43] Monserrat-Martinez, A.; Gambin, Y.; Sierecki, E. Thinking Outside the Bug: Molecular targets and strategies to overcome antibiotic resistance. International Journal of Molecular Sciences 2019, 20 (6), 1255. https://doi.org/10.3390/ijms20061255.

[44] Boyd, M. A.; Thavarajah, W.; Lucks, J. B.; Kamat, N. P. Robust and tunable performance of a cell-free biosensor encapsulated in lipid vesicles. Science Advances 2023, 9 (1). https://doi.org/10.1126/sciadv.add6605.

[45] Nelson, J. W.; Zhou, Z.; Breaker, R. R. Gramicidin D enhances the antibacterial activity of fluoride. Bioorganic & Medicinal Chemistry Letters 2014, 24 (13), 2969–2971. https://doi.org/10.1016/j.bmcl.2014.03.061.

[46] Choi, M. S.; Lee, C. Y.; Kim, J. H.; Lee, Y. M.; Lee, S.; Kim, H. J.; Heo, K. Gramicidin, a bactericidal antibiotic, is an antiproliferative agent for ovarian cancer cells. Medicina 2023, 59 (12), 2059. https://doi.org/10.3390/medicina59122059.

[47] (a) Kim, M.; Kang, N.; Ko, S.; Park, J.; Park, E.; Shin, D.; Kim, S.; Lee, S.; Lee, J.; Lee, S.; Ha, E.; Jeon, S.; Park, Y. Antibacterial and Antibiofilm Activity and Mode of Action of Magainin 2 against Drug-Resistant Acinetobacter baumannii. International Journal of Molecular Sciences 2018, 19 (10), 3041. https://doi.org/10.3390/ijms19103041.

(b) Lee, W.; Lee, D. G. Magainin 2 induces bacterial cell death showing apoptotic properties. Current Microbiology 2014, 69 (6), 794–801. https://doi.org/10.1007/s00284-014-0657-x.

[48] Pavlova, N.; Traykovska, M.; Penchovsky, R. Targeting FMN, TPP, SAM-I, and glmS Riboswitches with Chimeric Antisense Oligonucleotides for Completely Rational Antibacterial Drug Development. Antibiotics 2023, 12 (11), 1607. https://doi.org/10.3390/antibiotics12111607.

[49] Walker, M. J.; Varani, G. Design of RNA-targeting macrocyclic peptides. Methods in Enzymology on CD-ROM/Methods in Enzymology 2019, 339–372. https://doi.org/10.1016/bs.mie.2019.04.029.

[50] Pal, S.; Hart, P. 'T. RNA-Binding Macrocyclic peptides. Frontiers in Molecular Biosciences 2022, 9. https://doi.org/10.3389/fmolb.2022.883060.

[51] Mlýnský, V.; Kührová, P.; Pykal, M.; Krepl, M.; Stadlbauer, P.; Otyepka, M.; Banáš, P.; Šponer, J. Can We Ever Develop an Ideal RNA Force Field? Lessons Learned from Simulations of the UUCG RNA Tetraloop and Other Systems. Journal of Chemical Theory and Computation 2025. https://doi.org/10.1021/acs.jctc.4c01357.

[52] Šponer, J.; Krepl, M.; Banáš, P.; Kührová, P.; Zgarbová, M.; Jurečka, P.; Havrila, M.; Otyepka, M. How to understand atomistic molecular dynamics simulations of RNA and protein–RNA complexes? Wiley Interdisciplinary Reviews - RNA 2016, 8 (3). https://doi.org/10.1002/wrna.1405.

[53] Šponer, J.; Bussi, G.; Krepl, M.; Banáš, P.; Bottaro, S.; Cunha, R. A.; Gil-Ley, A.; Pinamonti, G.; Poblete, S.; Jurečka, P.; Walter, N. G.; Otyepka, M. RNA structural Dynamics as captured by molecular simulations: A Comprehensive Overview. Chemical Reviews 2018, 118 (8), 4177–4338. https://doi.org/10.1021/acs.chemrev.7b00427.

[54] Gray, J. G.; Case, D. A. Refinement of RNA structures using amber force fields. Crystals 2021, 11 (7), 771. https://doi.org/10.3390/cryst11070771.

[55] Cesari, A.; Bottaro, S.; Lindorff-Larsen, K.; Banáš, P.; Šponer, J.; Bussi, G. Fitting corrections to an RNA force field using experimental data. Journal of Chemical Theory and Computation 2019, 15 (6), 3425–3431. https://doi.org/10.1021/acs.jctc.9b00206.

[56] Kührová, P.; Mlýnský, V.; Zgarbová, M.; Krepl, M.; Bussi, G.; Best, R. B.; Otyepka, M.; Šponer, J.; Banáš, P. Correction to "Improving the performance of the amber RNA force field by tuning the Hydrogen-Bonding interactions." Journal of Chemical Theory and Computation 2019, 16 (1), 818–819. https://doi.org/10.1021/acs.jctc.9b01189.

[57] He, W.; Naleem, N.; Kleiman, D.; Kirmizialtin, S. Refining the RNA Force Field with Small-Angle X-ray Scattering of Helix–Junction–Helix RNA. The Journal of Physical Chemistry Letters 2022, 13 (15), 3400–3408. https://doi.org/10.1021/acs.jpclett.2c00359.

[58] Tan, D.; Piana, S.; Dirks, R. M.; Shaw, D. E. RNA force field with accuracy comparable to state-of-the-art protein force fields. Proceedings of the National Academy of Sciences 2018, 115 (7). https://doi.org/10.1073/pnas.1713027115.

[59] Vangaveti, S.; Ranganathan, S. V.; Chen, A. A. Advances in RNA molecular dynamics: a simulator's guide to RNA force fields. Wiley Interdisciplinary Reviews - RNA 2016, 8 (2). https://doi.org/10.1002/wrna.1396.

[60] Panteva, M. T.; Giambaşu, G. M.; York, D. M. Force Field for Mg2+, Mn2+, Zn2+, and Cd2+ Ions That Have Balanced Interactions with Nucleic Acids. The Journal of Physical Chemistry B 2015, 119 (50), 15460–15470. https://doi.org/10.1021/acs.jpcb.5b10423.

[61] Allnér, O.; Nilsson, L.; Villa, A. Magnesium Ion–Water coordination and exchange in biomolecular simulations. Journal of Chemical Theory and Computation 2012, 8 (4), 1493–1502. https://doi.org/10.1021/ct3000734.

[62] Grotz, K. K.; Cruz-León, S.; Schwierz, N. Optimized Magnesium Force Field Parameters for Biomolecular Simulations with Accurate Solvation, Ion-Binding, and Water-Exchange Properties. Journal of Chemical Theory and Computation 2021, 17 (4), 2530–2540. https://doi.org/10.1021/acs.jctc.0c01281.

[63] Sanbonmatsu, K. Y. Dynamics of riboswitches: Molecular simulations. Biochimica Et Biophysica Acta (BBA) - Gene Regulatory Mechanisms 2014, 1839 (10), 1046–1050. https://doi.org/10.1016/j.bbagrm.2014.06.010.

[64] Gilbert, S. D.; Batey, R. T. Monitoring RNA–Ligand interactions using isothermal titration calorimetry. Methods in Molecular Biology 2009, 97–114. https://doi.org/10.1007/978-1-59745-558-9_8.

[65] Moon, M. H.; Hilimire, T. A.; Sanders, A. M.; Schneekloth, J. S. Measuring RNA–Ligand Interactions with Microscale Thermophoresis. Biochemistry 2018, 57 (31), 4638–4643. https://doi.org/10.1021/acs.biochem.7b01141.

[66] Suddala, K. C.; Walter, N. G. Riboswitch Structure and Dynamics by SMFRET Microscopy. Methods in Enzymology on CD-ROM/Methods in Enzymology 2014, 343–373. https://doi.org/10.1016/b978-0-12-801122-5.00015-5.

[67] Ma, H.; Jia, X.; Zhang, K.; Su, Z. Cryo-EM advances in RNA structure determination. Signal Transduction and Targeted Therapy 2022, 7 (1). https://doi.org/10.1038/s41392-022-00916-0.

[68] Sun, A.; Huang, K.; Zheng, L.; Ren, A. Strategies for understanding RNA recognition by X-ray crystallography and NMR methods. Methods in Enzymology on CD-ROM/Methods in Enzymology 2019, 229–248. https://doi.org/10.1016/bs.mie.2019.05.024.

[69] Parmar, S.; Bume, D. D.; Connelly, C. M.; Boer, R. E.; Prestwood, P. R.; Wang, Z.; Labuhn, H.; Sinnadurai, K.; Feri, A.; Ouellet, J.; Homan, P.; Numata, T.; Schneekloth, J. S. Mechanistic analysis of Riboswitch Ligand interactions provides insights into pharmacological control over gene expression. Nature Communications 2024, 15 (1). https://doi.org/10.1038/s41467-024-52235-3.

[70] Kirchner, M.; Schorpp, K.; Hadian, K.; Schneider, S. An in vivo high-throughput screening for riboswitch ligands using a reverse reporter gene system. Scientific Reports 2017, 7 (1). https://doi.org/10.1038/s41598-017-07870-w.

[71] Hallberg, Z. F.; Su, Y.; Kitto, R. Z.; Hammond, M. C. Engineering and in vivo applications of riboswitches. Annual Review of Biochemistry 2017, 86 (1), 515–539. https://doi.org/10.1146/annurev-biochem-060815-014628.

[72] Sur, S.; Nimesh, H. Challenges and limitations of computer-aided drug design. Advances in Pharmacology 2025. https://doi.org/10.1016/bs.apha.2025.02.002.

[73] Ojha, D.; Rode, A. B. Rational development of FMN-based orthogonal riboswitch that functions in response to specific non-cognate ligand. Nature Communications 2025, 16 (1). https://doi.org/10.1038/s41467-025-60722-4.

[74] Shen, X.; Li, H.; Xu, X.; Song, Q.; Tai, X.; He, M.; Ren, A. Structure-based insights into the ligand specificity tuning of 2′-dG-III riboswitch. Nucleic Acids Research 2025, 53 (15). https://doi.org/10.1093/nar/gkaf773.

[75] Das, S. In silico studies on thermodynamics of ligand binding to Fluoride riboswitch aptamer. bioRxiv, 2024-06. https://www.biorxiv.org/content/10.1101/2024.06.23.600262v1